PROCEEDINGS OF SPIE

SPIEDigitalLibrary.org/conference-proceedings-of-spie

The Cryogenic Anti-Coincidence detector for ATHENA X-IFU: pulse analysis of the AC-S7 single pixel prototype

D'Andrea, M., Argan, A., Lotti, S., Macculi, C., Piro, L., et al.

M. D'Andrea, A. Argan, S. Lotti, C. Macculi, L. Piro, M. Biasotti, D. Corsini, F. Gatti, G. Torrioli, "The Cryogenic Anti-Coincidence detector for ATHENA X-IFU: pulse analysis of the AC-S7 single pixel prototype," Proc. SPIE 9905, Space Telescopes and Instrumentation 2016: Ultraviolet to Gamma Ray, 99055X (18 July 2016); doi: 10.1117/12.2231412

SPIE.

Event: SPIE Astronomical Telescopes + Instrumentation, 2016, Edinburgh, United Kingdom

Downloaded From: https://www.spiedigitallibrary.org/conference-proceedings-of-spie on 07 May 2020 Terms of Use: https://www.spiedigitallibrary.org/terms-of-use

The Cryogenic Anti-Coincidence detector for ATHENA X-IFU: pulse analysis of the AC-S7 single pixel prototype

M. D'Andrea*[a,b], A. Argan[a], S. Lotti[a], C. Macculi[a], L. Piro[a], M. Biasotti[c], D. Corsini[c], F. Gatti[c], G. Torrioli[d]

[a]INAF/IAPS Roma, Via del Fosso del Cavaliere 100, 00133 Roma (Italy);
[b]Dept. of Physics, Univ. of Rome "Tor Vergata",Via della Ricerca Scientifica 1,00133 Roma (Italy);
[c]Dept. of Physics, University of Genoa, Via Dodecaneso 33,16146 Genova (Italy);
[d]CNR/IFN Roma, Via Cineto Romano 42, 00156 Roma (Italy)

ABSTRACT

The ATHENA observatory is the second large-class mission in ESA Cosmic Vision 2015-2025, with a launch foreseen in 2028 towards the L2 orbit. The mission addresses the science theme "The Hot and Energetic Universe", by coupling a high-performance X-ray Telescope with two complementary focal-plane instruments. One of these is the X-ray Integral Field Unit (X-IFU): it is a TES based kilo-pixel order array able to provide spatially resolved high-resolution spectroscopy (2.5 eV at 6 keV) over a 5 arcmin FoV.

The X-IFU sensitivity is degraded by the particles background expected at L2 orbit, which is induced by primary protons of both galactic and solar origin, and mostly by secondary electrons. To reduce the background level and enable the mission science goals, a Cryogenic Anticoincidence (CryoAC) detector is placed < 1 mm below the TES array. It is a 4-pixel TES based detector, with wide Silicon absorbers sensed by Ir:Au TESes.

The CryoAC development schedule foresees by Q1 2017 the delivery of a Demonstration Model (DM) to the X-IFU FPA development team. The DM is a single-pixel detector that will address the final design of the CryoAC. It will verify some representative requirements at single-pixel level, especially the detector operation at 50 mK thermal bath and the threshold energy at 20 keV.

To reach the final DM design we have developed and tested the AC-S7 prototype, with 1 cm^2 absorber area sensed by 65 Ir TESes. Here we will discuss the pulse analysis of this detector, which has been illuminated by the 60 keV line from a ^{241}Am source.

First, we will present the analysis performed to investigate pulses timings and spectrum, and to disentangle the athermal component of the pulses from the thermal one. Furthermore, we will show the application to our dataset of an alternative method of pulse processing, based upon Principal Component Analysis (PCA). This kind of analysis allow us to recover better energy spectra than achievable with traditional methods, improving the evaluation of the detector threshold energy, a fundamental parameter characterizing the CryoAC particle rejection efficiency.

Keywords: ATHENA, Anticoincidence, Cryogenic detectors, TES, Pulse analysis, Principal Component Analysis

1. INTRODUCTION

ATHENA (Advanced Telescope for High Energy Astrophysics) is the second large-class mission selected in ESA Cosmic Vision 2015-2025, with a launch foreseen in 2028 towards the L2 orbit. The mission is designed to address the science theme "The Hot and Energetic Universe", answering some of the most pressing question in Astrophysics through X-ray observations (in the band 0.2–12 keV). ATHENA has considerably improved capabilities compared to all current or planned X-ray facilities and it will virtually affect all areas of Astrophysics[1].

The mission payload consists of a high-performance X-ray Telescope coupled to two complementary focal-plane instruments: the X-ray Integral Field Unit (X-IFU) and the Wide Field Imager (WFI). The X-IFU is a cryogenic X-ray spectrometer based on a large array of TES microcalorimeters, working at a base temperature of 50 mK. It will be the

*matteo.dandrea@iaps.inaf.it; phone +39 0649934379

Space Telescopes and Instrumentation 2016: Ultraviolet to Gamma Ray, edited by Jan-Willem A. den Herder, Tadayuki Takahashi, Marshall Bautz, Proc. of SPIE Vol. 9905, 99055X
© 2016 SPIE · CCC code: 0277-786X/16/$18 · doi: 10.1117/12.2231412

Downloaded From: https://www.spiedigitallibrary.org/conference-proceedings-of-spie on 07 May 2020
Terms of Use: https://www.spiedigitallibrary.org/terms-of-use

first X-ray instrument able to perform the so-called integral field spectroscopy, providing detailed images of its Field Of View (5' in diameter) with an angular resolution of 5" and fine energy spectra (resolution of 2.5eV at 6 keV)[2].

The X-IFU sensitivity is highly degraded by the particles background expected at L2 orbit, which is induced by primary protons, of both galactic and solar origin, and mostly by secondary electrons. Monte Carlo simulations show that to reduce the background level and enable the mission science goals it is necessary to adopt an active anti-coincidence device. To increase the rejection efficiency it must be placed less than 1 mm below the TES array, and so it must be cryogenic. Furthermore, it must have an accurate timing resolution to enable correlations with events in the main detector, and a trigger threshold below the typical energies deposited by background particles[3].

To meet these requirements we are developing the CryoAC: a Cryogenic AntiCoincidence detector based on TES technology, with four pixels composed of wide area Silicon absorbers sensed by a network of Ir:Au TESes. The CryoAC offers two principal advantages with respect other kinds of cryogenic detectors. First, it is based on the same technology of the main array, sharing with it thermal and mechanical interfaces, so increasing the Technology Readiness Level (TRL) of the X-IFU. Second, it will operate in an a-thermal regime, showing a fast component in the detection signal that can be efficiently used as fast anticoincidence flag. An overview of the CryoAC development program can be found in this issue[4], while details about the work done so far are reported in the references[5,6,7].

Here we will discuss the data analysis of AC-S7, the last CryoAC single pixel prototype developed by our consortium. We will present three different kind of pulse analysis, in increasing order of complexity: a raw analysis, a double pulse fitting procedure and a Principal Component Analysis. The aims of these procedures are respectively to preliminary investigate pulses timings and spectrum, to disentangle the athermal component of the pulses from the thermal one, and to recover the optimal energy spectrum.

2. THE AC-S7 DETECTOR: AN OVERVIEW

The AC-S7 prototype has been produced at the Physics Department of Genova University. It is constituted by 65 Iridium TESes uniformly distributed over 1 cm^2 Silicon absorber and connected in parallel through Nb lines (Fig. 1).

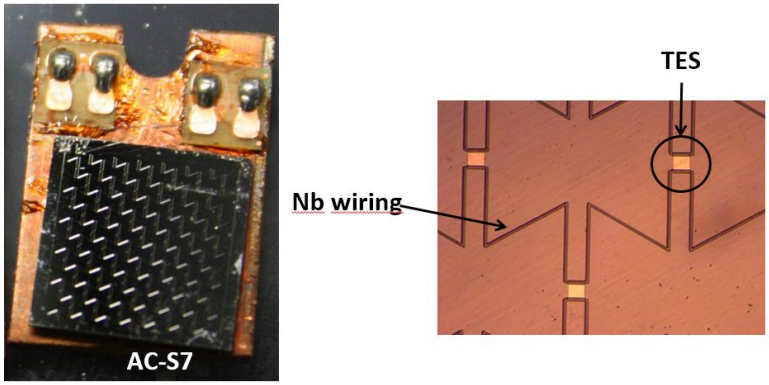

Figure 1. Left: the AC-S7 sample. Right: details about TESes and Nb wiring (Color figure online).

The main properties of the detector are shown in Table 1.

A very preliminary characterization of AC-S7 is reported in Ref. 7, while a more depth analysis of the I-V curves characteristics can be found in this issue[8]. Here we will focus on the pulse analysis, referring to the references for the electrothermal characterization of the sample.

Downloaded From: https://www.spiedigitallibrary.org/conference-proceedings-of-spie on 07 May 2020
Terms of Use: https://www.spiedigitallibrary.org/terms-of-use

Table 1. AC-S7 main properties.

AC-S7 MAIN PARAMETERS	
Parameter	Value
Absorber Silicon Area	10 x 10 mm^2
Absorber Silicon Thickness	380 μm
TES (x65) Iridium Area	100 x 100 μm^2
TES (x65) Iridium Thickness	~ 200 nm
T_C	~ 125 mK
ΔT_C	~ 2 mK
R_N	~ 1.5 mΩ
α_{max}	~ 100

3. PULSES RAW ANALYSIS

The detector has been illuminated with a ^{241}Am source, which was shielded to filter out the fluorescences and provide only the 60 keV line. For the TESes readout has been adopted a Supracon SQuID (model VCblue). The SQuID output has been filtered by a low noise band-pass 1Hz-10kHz and acquired with an ADC sampling rate of 100ks/s. The collected dataset - relative to about 2 hr of acquisition time - consists of 1270 pulses selected by a software trigger, each one containing 8000 samples. Some triggered pulses are shown in Fig. 2.

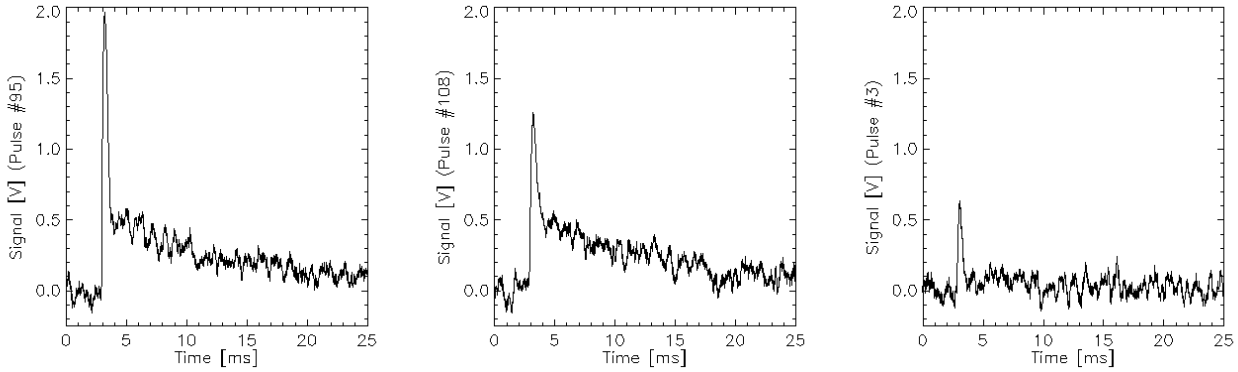

Figure 2. Examples of triggered pulses with different shapes.

The pulses clearly shows two different components, as expected for semiconductors absorbers at sub-K temperatures (see Ref. 5 and refs therein for details). The initial fast component is due to an out-of-equilibrium phonon family (the so-called 'athermal'), and it is developed before the usual thermal component, which is slower. The first two pulses in Fig. 2 show a similar thermal component and different athermal ones. In the third pulse only the athermal component is visible, while the thermal one is submerged in the noise.

A very raw analysis has been initially performed to know pulses timings and spectrum, in order to roughly understand how the detector works. The timing results are shown in Fig. 3-left. The 10%-90% rise time constant is well defined around the value of $\tau_{R,10\%-90\%}$ = (192 ± 62) μs, while the distribution of the 1/e decay times peaks around τ_D = (424 ± 85) μs, showing a tail to higher values attributable to the roughness of this kind of analysis and the noisy pulse shape. Note that the decay time here reported refers to the athermal component of the pulses, taking into account as reference the maximum value of the recorded data for each pulse.

In Fig. 3-right are shown the preliminary energy spectrum, represented by the distribution of the raw in-time integral of the pulses, and the Pulse Height distribution. The energy spectrum shows, as expected, a well-shaped principal line, corresponding to the 60 keV photopeak. The bump at lower energy is compatible with the correspondent Compton Edge

Downloaded From: https://www.spiedigitallibrary.org/conference-proceedings-of-spie on 07 May 2020
Terms of Use: https://www.spiedigitallibrary.org/terms-of-use

of 60 keV photons ($E_{CE,60keV}$ = 11.3 keV), whose shape is due to the convolution with the instrumental response. We remember that in Silicon the cross sections for photoelectric absorption and Compton scattering at 60 keV are quite similar ($\sigma_{PE,Si,60keV}$ = 0.13 cm^2/g ; $\sigma_{C,Si,60keV}$ = 0.15 cm^2/g)[9], and so we expect about half of the interacting photons in the Compton channel.

Lastly, note that the Pulse Height strongly depends on the athermal phonons collecting efficiency, and as a consequence the PH spectrum is less shaped than the raw in-time integral distribution. We will clarify this point later, with the double pulse fitting analysis.

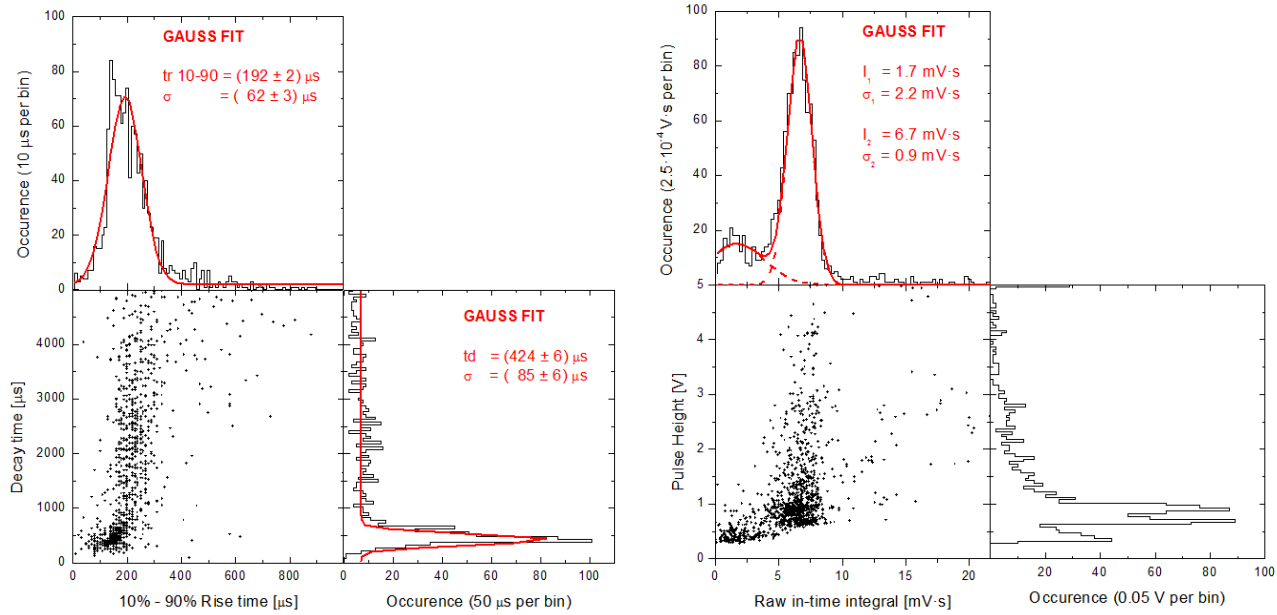

Figure 3. Left: Characteristic decay time vs 10%-90% rise time from the raw analysis. Right: Pulse Height spectrum vs raw in-time integral of the pulses (Color figure online).

4. DOUBLE PULSE FITTING PROCEDURE

The double pulse fitting procedure allow us to better investigate the detector dynamic, disentangling the athermal component of the pulses from the thermal one. Note that the athermal signal, being quite fast, is expected to be used as flag to reject the particle background, so it is important for us to characterize such a component.

The data shown in Fig. 2 show that the typical acquired pulses present the athermal rise and decay time constants close to each other, probably limited by the L/R filtering of the superconducting circuit. Hence, referring to Ref. 10 for the description of a pulse with a single time constant, we performed the double fit analysis by means of the equation:

$$P(t) = PH^{ath}\frac{t}{\tau^{ath}}e^{(1-t/\tau^{ath})} + PH^{th}\left(e^{-t/\tau_d{}^{th}} - e^{-t/\tau_r{}^{th}}\right) \quad , \quad \tau_r{}^{th} = \tau^{ath} \qquad (1)$$

where PH^{ath} is the athermal pulse height, τ^{ath} is the athermal peaking time, PH^{th} the thermal pulse height, $\tau_d{}^{th}$ the thermal decay time and $\tau_r{}^{th}$ the thermal rise time. The two time constants $\tau_r{}^{th}$ and τ^{ath} are assumed to be equivalent since the thermal phonon family rises while the athermal one decays, and this feature has been observed in several experiments[6]. An example of the fitting procedure is shown in Fig. 4.

Downloaded From: https://www.spiedigitallibrary.org/conference-proceedings-of-spie on 07 May 2020
Terms of Use: https://www.spiedigitallibrary.org/terms-of-use

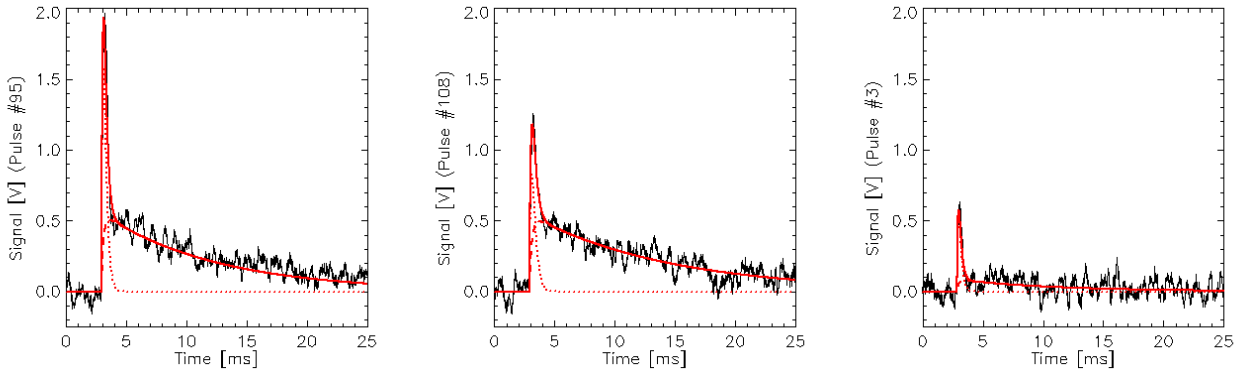

Figure 4. Results of the double pulse fitting procedure over the triggered pulses (s*olid red line*). *Dotted red line* and *dashed red line* respectively represent the athermal and the thermal component (Color figure online).

The next Fig. 5 shows the fitting parameters distributions.

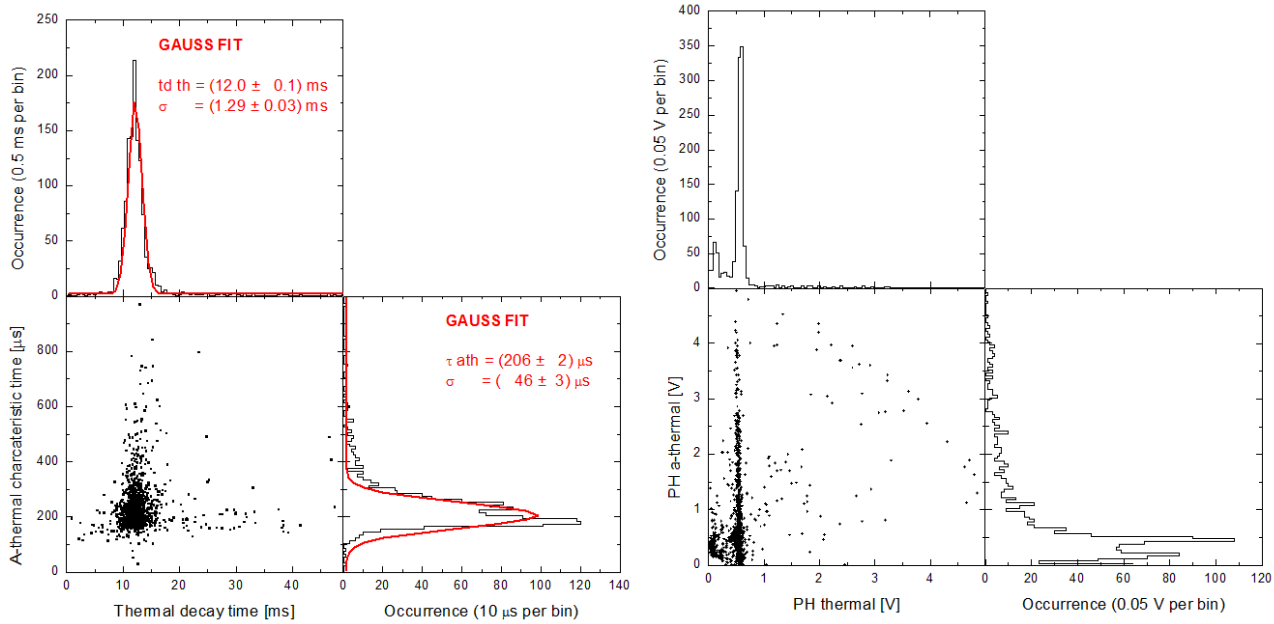

Figure 5. Left: Athermal characteristic time vs Thermal decay time from the double-pulse fitting procedure. Right: Athermal Pulse Height spectrum vs the thermal one (Color figure online).

The timing results are reported in Fig. 5-left. The thermal characteristic decay times show a Gaussian distribution with a central value of τ_d^{th} =12.0 ms and a small dispersion. The athermal peaking times are well defined around the value of τ^{ath} = (206 ± 46) μs, fully compatible with the 10%-90% rise-time from the raw analysis. Note also that given the functional form in eq. (1), the athermal 1/e decay time corresponds to about twice the peaking time, and so it is consistent with the results of the previous analysis (see Sect. 3).

In Fig. 5-right are shown the PH distributions. The spectra are plotted on the same scale to appreciate the difference between the thermal and athermal regimes. From the thermal point of view AC-S7 works fine in spectroscopic mode, providing both the 60 keV line and the expected Compton bump. The athermal regime shows a lower spectroscopic

Downloaded From: https://www.spiedigitallibrary.org/conference-proceedings-of-spie on 07 May 2020
Terms of Use: https://www.spiedigitallibrary.org/terms-of-use

capability, but the spectrum is still shaped, showing that the 65 TESes network is well working. The presence of two different lines in the athermal spectrum is currently under investigation but, roughly, it is probably an artifact due to the low signal-to-noise ratio for the lowest pulses. Note that the athermal spectrum shape has an impact on the raw "global" PH spectrum shown in Sect. 3 (Fig. 3-left), which therefore shows a low spectroscopic capability.

We conclude this section showing the distribution of the ratio between the athermal and the total (athermal + thermal) energy associated to each pulse (Fig. 6). The fraction of the athermal energy with respect to the total one is few %, in good agreement with the expected value for a Silicon absorber[11]. This is an important result that validates our analysis, enforcing that we are really detecting the athermal phonon population.

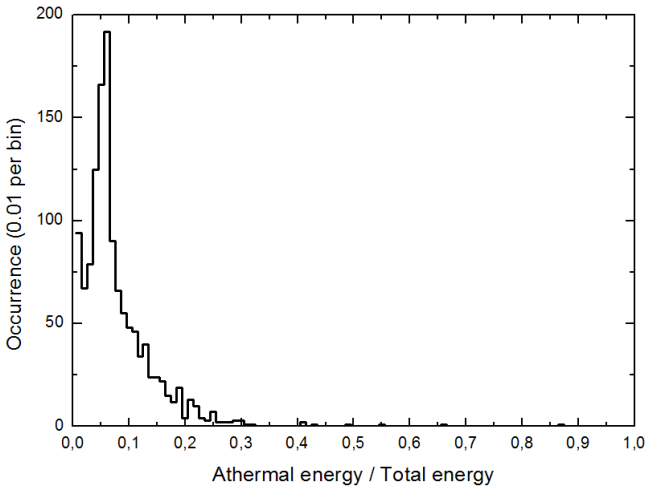

Figure 6. Distribution of the ratio between the athermal and the total (athermal + thermal) energy of the pulses.

5. PRINCIPAL COMPONENT ANALYSIS

In this section, we present a different approach for the pulses processing, based upon Principal Component Analysis (PCA). This kind of analysis requires no prior knowledge of the dataset and it has been successfully used to process cryogenic microcalorimeters signals with severe pulse shape variation, recovering better energy spectra than achievable with traditional analysis[12,13].

Principal Component Analysis is a statistical procedure that allows to represent a complex dataset in terms of a small set of orthogonal components that have the largest variance (Principal Components). It is widely used for data processing and dimensionality reduction in several research areas, from Neurosciences to Astronomy and Astrophysics. A simple introductive tutorial about PCA can be found in Ref. 14.

For the AC-S7 pulses processing we have followed the PCA implementation described in Ref. 13. The goal is to represent each pulse as the linear combination of the Principal Components of the signal, which are selected from the eigenvectors of the time covariance matrix of the pulses. In this way it is possible to identify the significant characteristic pulse shape components, filtering out the noise. The Principal Components can be then combined to form a representation of the pulses energy, obtaining the energy spectra.

5.1 PCA implementation

Here we describe step-by-step how we have implemented the PCA method to analyze the acquired pulses. The raw dataset consists of 1270 triggered pulse records, each one containing $N_S = 8000$ samples acquired with a sampling time $\Delta t = 10$ μs:

- We have picked out single (not piles-up) and non-saturated pulse records, selecting $N_P = 1207$ pulses (95% of all triggered events).

Downloaded From: https://www.spiedigitallibrary.org/conference-proceedings-of-spie on 07 May 2020
Terms of Use: https://www.spiedigitallibrary.org/terms-of-use

- We have defined the matrix DATA (N_S x N_P) containing all the selected pulses. Every column in the matrix contains a different event, so the matrix elements DATA[i,j] represents the j-th pulse at the i-th time in that pulse:

$$DATA = \begin{pmatrix} P_1(t=0) & P_2(t=0) & \cdots & P_{Np}(t=0) \\ P_1(t=\Delta t) & P_2(t=\Delta t) & \cdots & P_{Np}(t=\Delta t) \\ \vdots & \vdots & \cdots & \vdots \\ P_1(t=T) & P_2(t=T) & \cdots & P_{Np}(t=T) \end{pmatrix} \quad (2)$$

- We have created the data time covariance matrix COV (N_S x N_S), defined as:

$$COV = DATA \times (DATA)^T \quad (3)$$

- According to the PCA procedure, we want transform the data to a basis where the covariance matrix is diagonal:

$$COV = EV \times \Lambda \times (EV)^{-1} \quad (4)$$

where EV (N_S x N_S) is the matrix of eigenvectors and Λ is the diagonal matrix of eigenvalues (sorted from the highest to the lowest). We have therefore computed the eigenvalues and eigenvectors of the covariance matrix, using the DSYEV Fortran90 routine of the Linear Algebra PACKage[15].

- Finally, we have represented each pulse as the linear combination of the computed eigenvectors. To do this, we have rotated the pulses into the new basis EV:

$$R = (EV)^T \times DATA \quad (5)$$

The matrix R (N_S x N_P) contains the pulses projections onto all the eigenvectors, and so it is a complete alternative representation of our dataset.

5.2 Principal Components selection

Once obtained the projections matrix, the main task is to determine which eigenvectors are responsible for the shape of the pulses and which are encoding only noise-structures. Following Ref. 12, we identify the significant eigenvectors as the ones with the largest correspondent eigenvalues. The eigenvalues are indeed a measure of the information in the pulses encoded by the correspondent eigenvectors.

In Fig. 7 is shown the spectrum of the largest 100 eigenvalues that we have computed, and in Fig. 8 are plotted the first five eigenvectors with the respective histograms of the pulses projections. It is clear that the vast majority of the information regarding the pulses shape is encoded by the first two eigenvectors. Eigenvectors 3-4 encode some minor variations in the pulses, while the others contains no shape information and corresponds to the noise in the dataset.

It is interesting to note that the first eigenvector is essentially an average pulse. For the limit case of no pulse-shape variation, stationary noise and detector linear response, it would be the only representative eigenvector. Its projection histogram could then be used as representation of the energy spectrum, and the PCA should be equivalent to the conventional optimal filter.

In our case, we choose to select the first two eigenvectors to extract energy information from our dataset. We can see in Fig. 9 that these two components are sufficient to well describe the pulse shape and so, in first approximation, we can neglect the contribution of the subsequent eigenvectors.

Downloaded From: https://www.spiedigitallibrary.org/conference-proceedings-of-spie on 07 May 2020
Terms of Use: https://www.spiedigitallibrary.org/terms-of-use

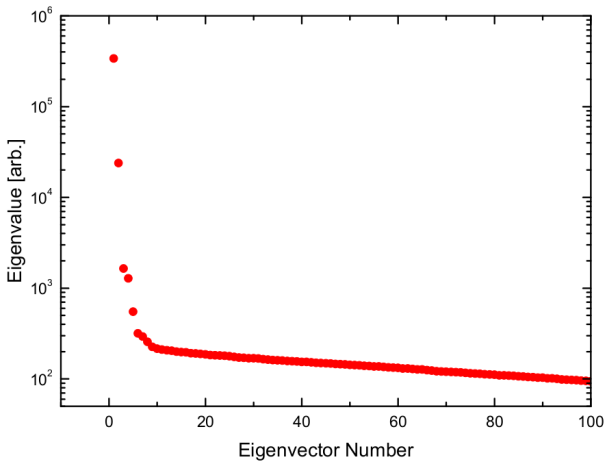

Figure 7. Spectrum of the largest 100 eigenvalues of the covariance matrix (Color figure online).

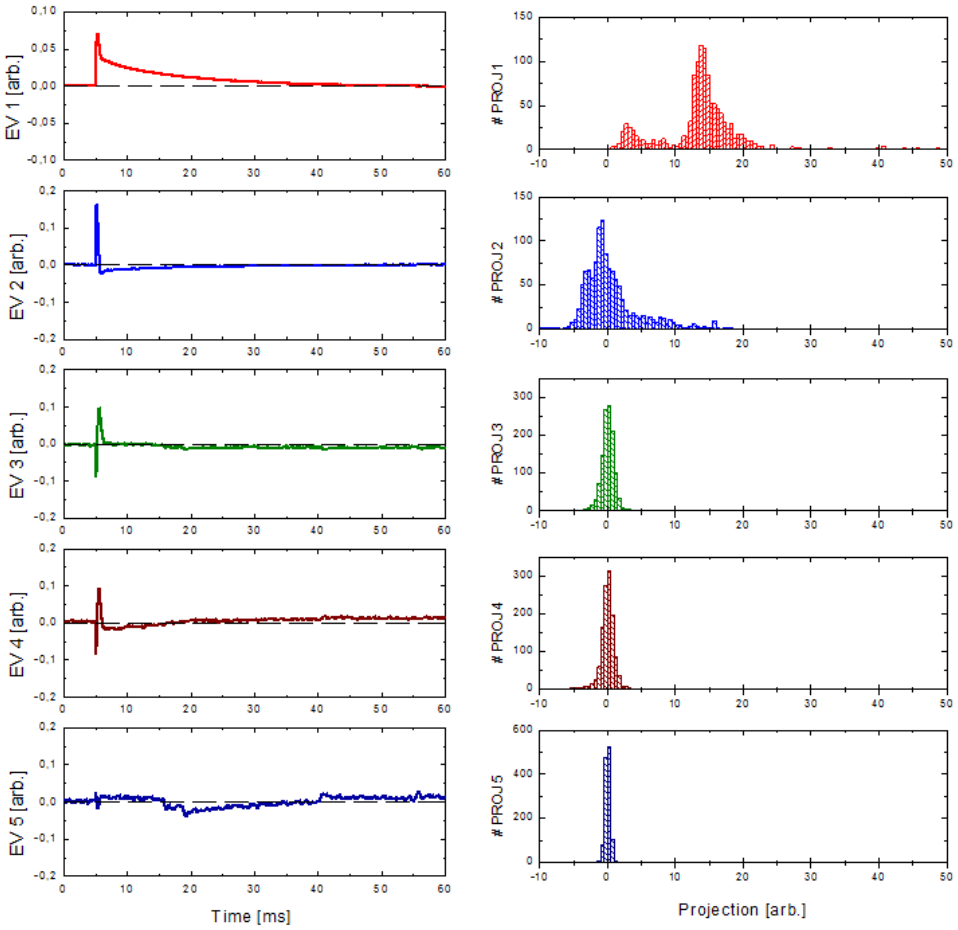

Figure 8. Left: The first five eigenvectors of the pulses covariance matrix. Right: Histogram of the projections of the pulses onto the correspondent (left) eigenvector (Color figure online).

Downloaded From: https://www.spiedigitallibrary.org/conference-proceedings-of-spie on 07 May 2020
Terms of Use: https://www.spiedigitallibrary.org/terms-of-use

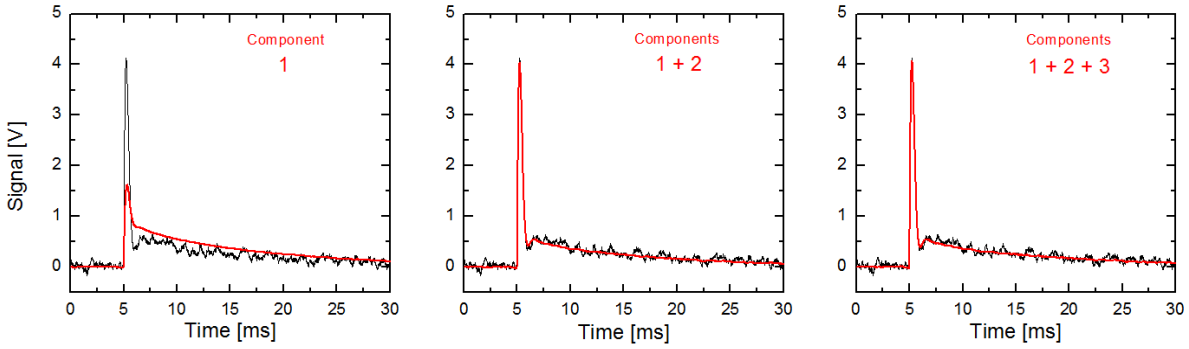

Figure 9. An example raw pulse (black line) in comparison with the correspondent PCA reconstruction (red line) for an increasing number of considered components (Color figure online).

To obtain the energy spectra we have examined the 2D scatter plot of the pulses projections onto the two selected eigenvectors (Fig.10).

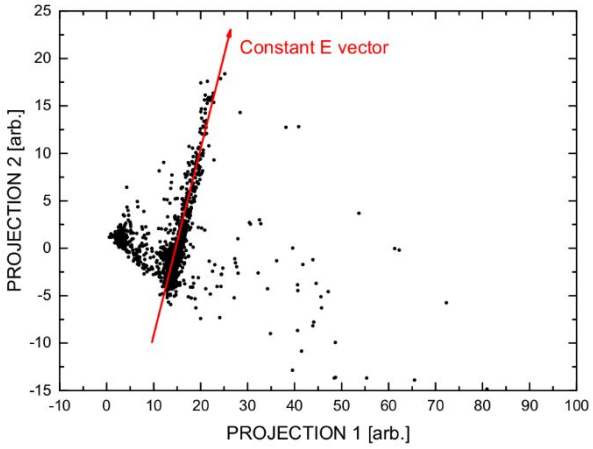

Figure 10. 2D scatter plot of the projections of each pulse onto the first two eigenvectors. The red arrow indicates, as labeled, the constant energy direction (Color figure online).

Every black point in the plot represents a different pulse. We can associate the principal cluster of points to the 60 keV line that we mainly expect from the ^{241}Am source, determining the direction of constant energy in the 2D projections space. Following the prescription in Ref. 13, this direction defines an axis that we have used as reference y-axis to rotate the scatter plot, putting the cluster vertical. We then used the projection onto the new x-axis (which is perpendicular to the constant E vector, and so it represents the ΔE direction) to generate the energy histogram of the pulses.

5.3 Energy spectra comparison

The energy spectrum obtained from the PCA is shown in Fig. 11, in comparison with the spectra from the raw and the double pulse fitting analysis. All the spectra have been calibrated to the 60 keV line and fitted with a double peak Gaussian function.

Downloaded From: https://www.spiedigitallibrary.org/conference-proceedings-of-spie on 07 May 2020
Terms of Use: https://www.spiedigitallibrary.org/terms-of-use

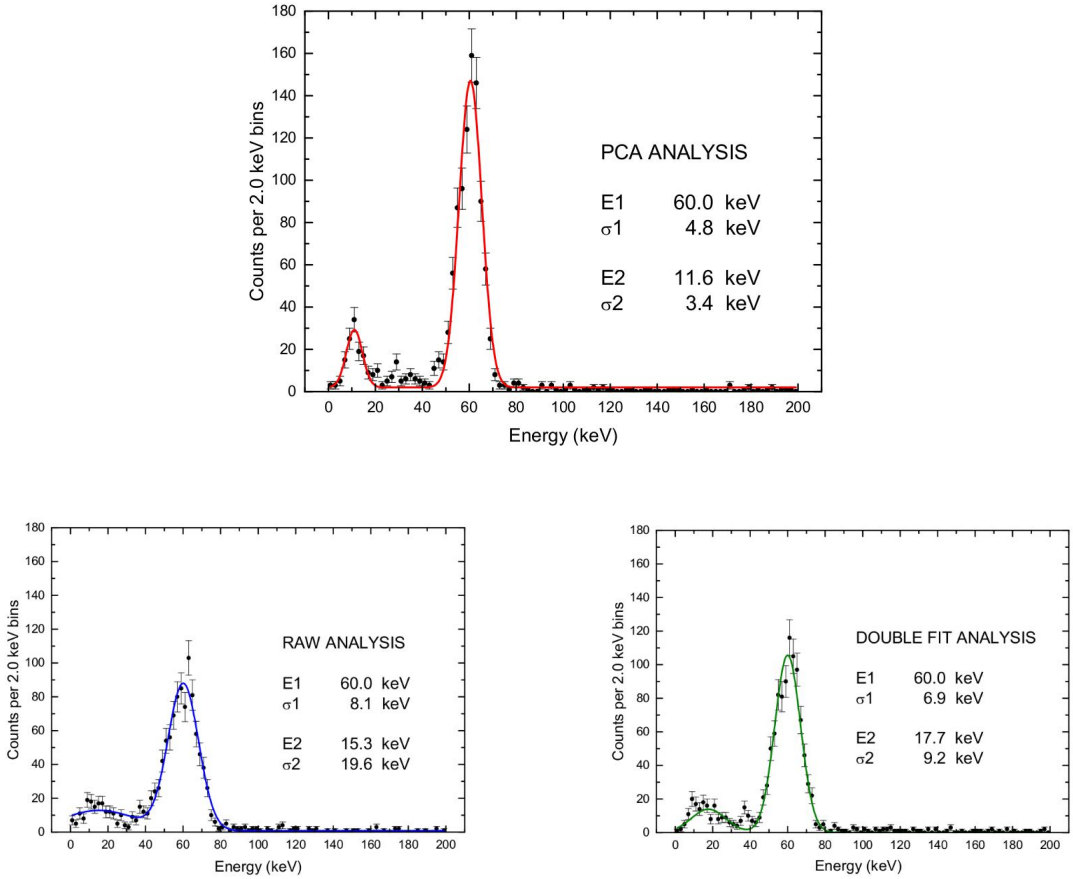

Figure 11. *Top:* Energy spectrum from the P CA technique. *Bottom:* Energy spectra from the raw analysis (*left*) and the double pulse fitting procedure (*right*). (Color figure online).

The PCA technique provides a more narrow 60 keV line, improving the spectral resolution of a factor 1.4 compared to the fit procedure and of a factor 1.7 with respect to the raw analysis. Also the bump at lower energy is better shaped, enforcing the hypothesis that we are observing the Compton edge expected at 11.3 keV. Further investigations will be carried out at these energies in the next future.

Although the CryoAC is not aimed to perform spectroscopy, improving the energy resolution is a remarkable result because it enable us to better determine the threshold energy of the detector. This parameter is important to reach high particle rejection efficiency (the wider the detector energy bandwidth, the higher the particle flux the CryoAC is able to veto), and so it must be well characterized. From the PCA spectrum is possible to evaluate for AC-S7 a threshold of about 20 keV, fully compatible with our requirements[4].

6. CONCLUSIONS

In this work we have reported the pulses analysis performed on AC-S7, a single-pixel TES based prototype developed for the Cryogenic Anticoincidence detector of ATHENA X-IFU. The sample has been illuminated by a ^{241}Am source, providing a dataset of 1270 pulses. We have performed three different kind of analysis: a raw analysis, a double pulse fitting procedure and a Principal Component Analysis.

Downloaded From: https://www.spiedigitallibrary.org/conference-proceedings-of-spie on 07 May 2020
Terms of Use: https://www.spiedigitallibrary.org/terms-of-use

The raw analysis provided us a well-shaped energy spectrum: the main 60 keV photopeak line is clearly defined and a little bump around 10 keV is compatible with the correspondent expected Compton Edge ($E_{CE,60keV}$ = 11.3 keV).

With the double pulse fitting we have disentangled the athermal component of the pulses from the thermal one. Timing results are fully compatible with the ones from the raw analysis, so validating the fit procedure. The athermal-to-total energy ratio is consistent to what expected for Silicon (few percent), showing that the athermal phonon collection is efficiently performed by the TESes network.

Finally, through an alternative method of pulse processing based upon PCA, we have obtained an optimal energy spectrum, improving the resolution of a factor 1.4 compared to the fit procedure and of a factor 1.7 with respect to the raw analysis. This has allowed us to better evaluate the energy threshold of the detector of about 20 keV, compatible with our requirements.

ACKNOWLEDGEMENT

This work has been supported by ASI (Italian Space Agency) through the Contract n. 2015-046-R.0.

REFERENCES

[1] Nandra, K., Barret, D., Barcons, X., Fabian, A., den Herder, J.-W., Piro, L., Watson, M., et al., "The Hot and Energetic Universe: A White Paper presenting the science theme motivating the Athena+ mission," 2013arXiv1306.2307N (2013).
[2] Barret, D., den Herder, J.-W., Piro, L., Trong, T. L., Barcons, X., "The ATHENA X-ray Integral Field Unit," in this issue, paper 9905-83 (2016).
[3] Lotti, S., Perinati, E., Natalucci, L., Piro, L., Mineo, T., Colasanti, L., Macculi, C., Federici, M., Martino, B., "An efficient method for reducing the background of microcalorimeters applied to ATHENA-XMS," Proc. of SPIE 8443 (2012).
[4] Macculi, C., et al., "The Cryogenic AntiCoincidence Detector Project for ATHENA X-IFU: a program overview," in this issue, paper 9905-88 (2016)
[5] Macculi, C., et al., "The Cryogenic AntiCoincidence Detector Project for ATHENA+: An Overview Up to the Present Status," J Low Temp Phys 176 (2014).
[6] Macculi, C., et al., "The Cryogenic AntiCoincidence detector for ATHENA: the progress towards the final pixel design," Proc. of SPIE 9144 (2014).
[7] Macculi, C., et al., "The Cryogenic AntiCoincidence detector for the ATHENA X-IFU: design aspects by Geant4 simulation, and preliminary characterization of the new single pixel," J Low Temp Phys, DOI 10.1007/s10909-015-1439-y (2016).
[8] Biasotti, M., et al., "The new cryogenic silicon monolithic micro-bridged AntiCoincidence detector for the X-IFU of ATHENA," in this issue, paper 9905-187 (2016).
[9] Berger, M.J., Hubbell, J.H., Seltzer, S.M., Chang, J., Coursey, J.S., Sukumar, R., Zucker, D.S., and Olsen, K., "XCOM: Photon Cross Section Database (version 1.5)," Online Available: http://physics.nist.gov/xcom (2010)
[10] Irwin, K. D., Hilton, G. C. , "Transition-Edge Sensors," Topics Appl. Phys. 99, 63-149 (2005)
[11] Msall, M.E., Wolfe, J.P., "Ballistic phonon production in photoexcited Ge, GaAs, and Si," Physical Review B 65, 195205 (2002)
[12] Bush, S.E., et al., "Progress Towards Improved Analysis of TES X-ray Data Using Principal Component Analysis," J Low Temp Phys, DOI: 10.1007/s10909-015-1357-z (2015)
[13] Yan, D., et al., "Processing of X-Ray Microcalorimeter Data with Pulse Shape Variation using Principal Component Analysis," J Low Temp Phys, DOI: 10.1007/s10909-016-1480-5 (2016)
[14] Shlens, J., "A Tutorial on Principal Component Analysis," arXiv:1404.1100 (2014)
[15] Anderson, E., Bai, Z., Bischof, C., Blackford, S., Demmel, J., Dongarra, J., Du Croz, J., Greenbaum, A., Hammarling, S.,McKenney, A., Sorensen, D., "LAPACK Users Guide," Society for Industrial and Applied Mathematics, Third edition (1999)

Downloaded From: https://www.spiedigitallibrary.org/conference-proceedings-of-spie on 07 May 2020
Terms of Use: https://www.spiedigitallibrary.org/terms-of-use